THE

PHYSICAL REVIEW

A journal of experimental and theoretical physics established by E. L. Nichols in 1893

SECOND SERIES, VOL. **181**, NO. 3 15 MAY 1969

Band Structure and Fermi Surface of ReO_3

L. F. MATTHEISS

Bell Telephone Laboratories, Murray Hill, New Jersey 07974

(Received 2 December 1968)

The nonrelativistic augmented-plane-wave (APW) method has been applied to calculate the band structure of ReO_3. An important feature of this calculation is that it includes corrections to the usual "muffin-tin" approximation. Because of convergence difficulties, the APW calculation has been carried out only at symmetry points in the Brillouin zone. These results have been used in conjunction with the Slater-Koster linear-combination-of-atomic-orbitals interpolation scheme to determine the band structure and Fermi surface throughout the Brillouin zone. The Fermi energy occurs in the t_{2g} manifold of the rhenium $5d$ bands. The calculation predicts a Fermi surface consisting of two closed electron sheets centered about Γ, plus a third electron sheet which is open along $\langle 100 \rangle$. The tight-binding parameters, which affect both the oxygen-rhenium ($2p$-$5d$) energy separation and the corresponding bandwidths, have been adjusted to fit the optical and Fermi-surface data for ReO_3. Spin-orbit effects for the rhenium $5d$ bands have been included by means of a spin-orbit parameter ξ_{5d}. The optimum value for this parameter has been determined by detailed comparisons between the theoretical and experimental Fermi-surface areas. The final results agree to within 10%.

I. INTRODUCTION

THE transition-metal oxides exhibit a rich variety of electrical and magnetic properties which are interesting from a fundamental as well as a practical point of view. These properties include the semiconductor-to-metal transitions in the lower oxides of titanium and vanadium[1] as well as the various types of magnetic ordering which are found to exist in other examples of these materials.[2,3]

Compared to these more exotic transition-metal oxides, the electrical and magnetic properties of rhenium trioxide (ReO_3) can only be described as "ordinary." ReO_3 is nonmagnetic and exhibits metallic-type conductivity down to liquid-helium temperatures. The importance of ReO_3 arises from the growing wealth of experimental data relating to the electronic energy bands. The optical measurements of Feinleib *et al.*[4] provide band-structure information over a 22-eV energy range. Recently, Marcus[5] has observed de Haas–van Alphen oscillations in single-crystal samples of this compound. These results provide important and detailed information concerning the ReO_3 band structure at the Fermi energy. More recently, magnetothermal oscillations have been observed in ReO_3 samples by Graebner.[6] His data are in basic agreement with Marcus's de Haas–van Alphen results.

The purpose of the present investigation is to determine a theoretical model for the ReO_3 band structure which is consistent with both the Fermi surface and the optical data. The calculations leading to this model have been carried out in three stages. The first stage involves a nonrelativistic augmented-plane-wave (APW) calculation for ReO_3 at symmetry points in the Brillouin zone. This calculation assumes an *ad hoc* potential which is derived from *neutral* atom charge densities. An important feature of this calculation is that it includes corrections to usual muffin-tin approximation to the crystal potential.[7]

In the second stage of the calculation, the Slater-Koster LCAO (linear-combination-of-atomic-orbitals) interpolation scheme has been fitted to the APW results at symmetry points to determine the energy bands throughout the Brillouin zone.[8] This fitting procedure has included states arising from the rhenium $5d$ and

---

[1] F. J. Morin, Phys. Rev. Letters **3**, 34 (1959).

[2] J. B. Goodenough, *Magnetism and the Chemical Bond* (Wiley-Interscience, Inc., New York, 1963).

[3] *Transition Metal Compounds*, edited by E. Schatz (Gordon and Breach Science Publishers, Inc., New York, 1964).

[4] J. Feinleib, W. J. Scouler, and A. Ferretti, Phys. Rev. **165**, 765 (1968).

[5] S. M. Marcus, Phys. Letters **27A**, 584 (1968).

[6] J. E. Graebner (unpublished).

[7] P. D. DeCicco, Phys. Rev. **153**, 931 (1967).

[8] J. C. Slater and G. F. Koster, Phys. Rev. **94**, 1498 (1954).

oxygen $2p$ bands. The bands arising from the rhenium $6s$-$6p$ and the oxygen $2s$ atomic levels have been omitted from this interpolation calculation. The effects of spin-orbit coupling among the rhenium $5d$ states have been taken into account by means of a spin-orbit parameter ξ_{5d}. The results of these calculations are in good qualitative agreement with the Fermi-surface and optical data.

In the final stage of the calculation, the LCAO or tight-binding parameters which affect the energy separation between the (lower) oxygen $2p$ and (higher) rhenium $5d$ energy band states as well as the corresponding bandwidths have been adjusted in accordance with the optical[4] and cyclotron mass[5] data. The Fermi-surface areas obtained from this adjusted band structure agree with the experimental results to within 10%.

The general arrangement of this paper is as follows. The details of the calculation are described in Sec. II. This discussion includes a general description of the ReO_3 structure, the calculation of the one-electron potential, the corrections to the muffin-tin potential, and the details of the tight-binding calculation. The results of the calculation are presented in Sec. III, including energy-band, density-of-states, and Fermi-surface information. These results are compared with experiment in Sec. IV. The last section contains a general discussion of the present model for the ReO_3 band structure and its relationship to previous models that have been proposed for ReO_3 and structurally related materials.

II. DETAILS OF THE CALCULATION

A. ReO_3 Structure

An important aspect of ReO_3 is determined by its similarity to the perovskites ABC_3. The simple cubic ReO_3 unit cell is shown in Fig. 1(a). The more heavily shaded Re atom (ion) is located at the origin, while the more lightly shaded O atoms (ions) occupy positions at the face centers. In the perovskites, the Re and O atoms are replaced by the B and C atoms, respectively, while the A atoms are situated at the corners of the cube. Another related class of materials is represented by the tungsten bronzes, including compounds such as Na_xWO_3.

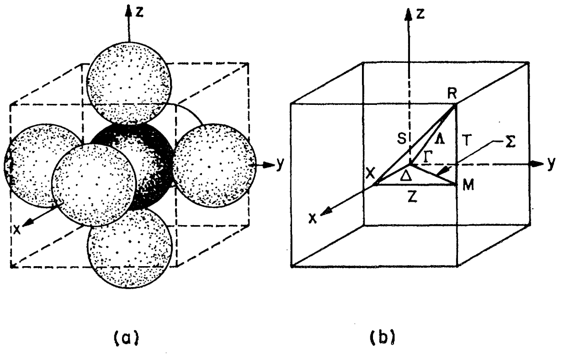

(a) (b)

FIG. 1. (a) Unit cell for the ReO_3 structure. (b) Brillouin zone for the simple cubic bravais lattice.

According to Fig. 1(a), the ReO_3 unit cell contains a single ReO_3 complex. The bravais lattice is simple cubic; the appropriate Brillouin zone is shown to the right in Fig. 1(b), where the standard notation is used to designate various symmetry points (Γ,X,M,R) and lines ($\Delta,\Sigma,\Lambda,S,T,Z$).[9] The space group for the ReO_3 structure is $O_h{}^1$, which is a symmorphic space group. The irreducible representations for this space group are available in the literature.[9] The rhenium atom is situated at a site with full cubic (O_h) point symmetry. The oxygen atoms reside at sites with tetragonal (D_{4h}) point symmetry.

In sorting out the energy-band results, it is useful to know which spherical harmonics centered about the rhenium and oxygen sites contribute to energy band states of a given symmetry. This information is readily determined by considering the transformation properties of Bloch-type functions formed from s, p, and d atomic-type orbitals centered about the rhenium and oxygen sites, respectively. Using familiar group-theoretical techniques, the appropriate symmetry of the energy-band states which arise from these atomic levels can be determined. This information is summarized in Table I for the ReO_3 structure.

ReO_3 contains a single rhenium atom per unit cell. This atom produces a single s band, three p bands, and five d bands, as expected. This is consistent with the results shown in Table I when the degeneracies of the various irreducible representations are taken into account. On the other hand, the three oxygen atoms in the ReO_3 unit cell produce three s bands, nine p bands, and a possible 15 d-band states. Because of oxygen's position in the periodic table, the oxygen d states represent highly excited levels, both in the atom as well as in the solid.

B. APW Calculation

The ReO_3 structure is not ideally suited to a straightforward application of the APW method, which involves the muffin-tin potential approximation. This is due to the fact that ReO_3 is a rather open or loosely-packed structure when compared to the fcc or hcp structures, for example.[10] However, DeCicco has suggested a means for correcting these deficiencies in the method.[7] He suggests decomposing the crystal potential $V(\mathbf{r})$ into a muffin-tin part $V_m(\mathbf{r})$ plus corrections $V_\Delta(\mathbf{r})$, so that

$$V(\mathbf{r})=V_m(\mathbf{r})+V_\Delta(\mathbf{r}). \qquad (1)$$

The muffin-tin potential $V_m(\mathbf{r})$ is one which is spherically symmetric inside the APW sphere centered about

---

[9] L. P. Bouckaert, R. Smoluchowski, and E. Wigner, Phys. Rev. **50**, 58 (1936).

[10] L. F. Mattheiss, J. H. Wood, and A. C. Switendick, Methods Comput. Phys. **8**, 64 (1968).

TABLE I. Spherical harmonic content of ReO_3 energy-band states at the symmetry points Γ, X, M, and R in the Brillouin zone. Entries include states arising from s, p, and d atomic-type orbitals centered about the rhenium and oxygen sites, respectively.

	Γ	X	M	R
			Rhenium states	
s	Γ_1	X_1	M_1	R_1
p	Γ_{15}	$X_{4'}+X_{5'}$	$M_{4'}+M_{5'}$	R_{15}
d	$\Gamma_{12}+\Gamma_{25'}$	$X_1+X_2+X_3+X_5$	$M_1+M_2+M_3+M_5$	$R_{12}+R_{25'}$
			Oxygen states	
s	$\Gamma_1+\Gamma_{12}$	$X_1+X_2+X_{4'}$	$M_1+M_{5'}$	R_{15}
p	$2\Gamma_{15}+\Gamma_{25}$	$X_1+X_5+X_{3'}+X_{4'}+2X_{5'}$	$M_1+M_2+M_3+M_4$ $+M_5+M_{4'}+M_{5'}$	$R_1+R_{12}+R_{25'}+R_{15'}$
d	$\Gamma_1+\Gamma_2+2\Gamma_{12}$ $+2\Gamma_{25'}+\Gamma_{15'}$	$2X_1+2X_2+X_3+X_4+2X_5$ $+X_{1'}+X_{3'}+X_{4'}+X_{5'}$	$M_1+M_2+M_3+M_5+M_{1'}+M_{2'}$ $+M_{3'}+M_{4'}+3M_{5'}$	$R_{2'}+R_{12'}+2R_{15}+2R_{25}$

each atomic site and constant throughout the remainder of the unit cell. Although the sphere radii are arbitrary, the convergence of the method is improved by making the spheres as large as possible (i.e., touching).[10]

If $V_\Delta(\mathbf{r})$ is zero within each sphere, these corrections can be incorporated *exactly* into the APW method by adding a single additional term to the usual APW matrix elements, namely, the Fourier coefficient of $V_\Delta(\mathbf{r})$:

$$V_\Delta(\mathbf{K}_j-\mathbf{K}_i)=\Omega^{-1}\int_{\text{cell}} \exp[-i(\mathbf{k}+\mathbf{K}_j)\cdot\mathbf{r}]V_\Delta(\mathbf{r}) \times\exp[i(\mathbf{k}+\mathbf{K}_i)\cdot\mathbf{r}]d^3r, \quad (2)$$

where Ω is the unit cell volume, $\mathbf{k}$ is a wave vector in the first Brillouin zone, and $\mathbf{K}_l$ equals a vector of the reciprocal lattice multiplied by 2π. In general, $V_\Delta(\mathbf{r})$ is not zero within the APW spheres; DeCicco has suggested two approximate methods for estimating the effects of such corrections under these circumstances.

The sphere radii used in the present APW calculation for ReO_3 are listed in Table II, along with the appropriate lattice parameter.[11] These sphere radii were chosen to produce touching oxygen and rhenium spheres along $\langle 100\rangle$ and to optimize the convergence of both the oxygen $2p$ and rhenium $5d$ bands.[10] Despite this precaution, the APW calculation requires approximately 250 APW functions in order to yield energy-band results which converge to within about 0.001 Ry. This fact precludes the possibility of carrying out APW calculations at general points in the Brillouin zone and even inhibits accurate calculations along symmetry lines. As a result, we have confined the APW calculations to the symmetry points Γ, X, M, and R, where group-theoretical techniques permit one to factor the resulting secular equations and reduce them to more manageable size.

The crystal potential $V(\mathbf{r})$ was approximated by an *ad hoc* potential derived from Hartree-Fock-Slater (HFS) atomic charge densities.[12] The Coulomb potential $V_c(\mathbf{r}_i)$ at an arbitrary point $\mathbf{r}_i$ in the unit cell was calculated by summing directly the contributions from neighboring Re and O atoms. The total charge density $\rho(\mathbf{r}_i)$ was calculated in this same manner. The total potential $V(\mathbf{r}_i)$ contained the Coulomb term $V_c(\mathbf{r}_i)$ plus the Slater exchange contribution, $-6[3\rho(\mathbf{r}_i)/8\pi]^{1/3}$, or

$$V(\mathbf{r}_i)=V_c(\mathbf{r}_i)-6[3\rho(\mathbf{r}_i)/8\pi]^{1/3}. \quad (3)$$

The spherically symmetric portions of the muffin-tin potential were determined by calculating $V(\mathbf{r}_i)$ along three independent directions originating from the rhenium and oxygen sites, respectively, and extending to the appropriate sphere radii. A weighted average of these results determined the spherically symmetric portions of $V_m(\mathbf{r})$. To determine the constant portion of $V_m(\mathbf{r})$ outside the spheres, V_{mo}, the potential $V(\mathbf{r}_i)$ was averaged over a uniformly distributed three-dimensional grid of points $\mathbf{r}_i$ equivalent to 17 576 points in the entire unit cell.

The differences between $V(\mathbf{r}_i)$ and V_{mo} were used to calculate the Fourier coefficients $V_\Delta(\mathbf{K}_l)$. This was done by direct summation,

$$V_\Delta(\mathbf{K}_l)=N^{-1}\sum_{n=1}^{N} e^{i\mathbf{K}_l\cdot\mathbf{r}_n}[V(\mathbf{r}_n)-V_{mo}], \quad (4)$$

where N is the total number of points in the unit cell at which $V(\mathbf{r}_n)$ was calculated. Those Fourier coefficients for which $\mathbf{K}_l=(2\pi/a)(l_1,l_2,l_3)$ and $0\leq(l_1,l_2,l_3)\leq 6$ were calculated and included in the APW calculation. The Fourier series converged rather slowly; typical values of $V_\Delta(\mathbf{K}_l)$ ranged from -0.1276 Ry for $\mathbf{K}_1=(2\pi/a)$ $(1,0,0)$ to -0.0006 Ry for $\mathbf{K}_{84}=(2\pi/a)(6,6,6)$.

In the present APW calculations for ReO_3, the corrections to the muffin-tin potential inside the APW spheres have been neglected. The effect of these cor-

TABLE II. Summary of the structure-related parameters involved in the APW calculation for ReO_3.

Lattice parameter a	7.0705 a.u.
Rhenium sphere radius R_s(Re)	1.9035 a.u.
Oxygen sphere radius R_s(O)	1.6317 a.u.
Fraction of unit cell outside APW spheres	0.764

---

[11] W. B. Pearson, in *A Handbook of Lattice Spacings and Structures of Metals and Alloys* (Pergamon Press, Inc., New York, 1958).

[12] F. Herman and S. Skillman, *Atomic Structure Calculations* (Prentice-Hall, Inc., Englewood Cliffs, N. J., 1963).

rections on the band structure is expected to be small. The corresponding corrections outside the APW spheres are quite large in ReO_3, ranging from -2.05 Ry in the region where the Re and O spheres contact to $+0.68$ Ry at $\frac{1}{2}(a,a,a)$. This peak-to-peak variation is roughly six times larger than that found by DeCicco in his KCl calculation.[7]

C. Tight-Binding Calculation

The convergence difficulties resulting from the application of the APW method to transition-metal compounds such as ReO_3 limit the usefulness of this method for determining the details of the band structure and Fermi surface throughout the Brillouin zone. As a result, we have applied the LCAO or tight-binding interpolation scheme of Slater and Koster for this purpose.[8] This scheme is readily adapted to include the effects of spin-orbit coupling, as we shall show presently.

The LCAO scheme has been applied by Kahn and Leyendecker to determine the band structure for the structurally related compound $SrTiO_3$.[13] In the present application of this method, the APW results at Γ, X, M, and R have been used to determine the various transfer integrals which enter the scheme as disposable parameters. In the Kahn-Leyendecker calculation, these parameters were estimated from a variety of sources, including experimental data, model calculations, and symmetry arguments. More recently, a complete LCAO tight-binding formalism for the ReO_3 structure has been worked out by Honig *et al.*[14] This formalism has been developed independently by the present author (though in less complete form) during the course of the present investigation.

The detailed form of the LCAO tight-binding interpolation scheme which has been applied to the present ReO_3 band-structure calculations is contained in Table III. This application of the method involves a total of 14 basis functions. These include five rhenium $5d$ orbitals and nine oxygen $2p$ orbitals, as specified in Table III A. The nonvanishing *d-d*, *p-p*, and *p-d* Hamiltonian matrix elements are contained in Table III B–III D, respectively.

The calculation includes nearest-neighbor rhenium-rhenium (*d-d*) interactions, nearest-neighbor and second nearest-neighbor oxygen-oxygen (*p-p*) interactions, and nearest-neighbor oxygen-rhenium (*p-d*) interactions. According to the results of Table III, these interactions are represented by a total of 19 parameters; six parameters (D_1–D_6) describe the *d-d* interactions, 11 (A_1–C_4) represent the *p-p* interactions, and two (P_1,P_2) include *p-d* hybridization effects in the model. The 11 *p-p* parameters can be described more precisely. The parameters A_1–A_3 enter the diagonal matrix elements of the oxygen $2p\sigma$ orbitals, while B_1–B_4 enter the di-

TABLE III. Tabulation of nonzero tight-binding Hamiltonian matrix elements, as used in the ReO_3 interpolation calculation, where $\xi=k_xa$, $\eta=k_ya$, and $\zeta=k_za$.

A. Tight-binding basis functions

	No.	Origin	Function
Rhenium d	1	(0,0,0)	xy
	2	(0,0,0)	yz
	3	(0,0,0)	zx
	4	(0,0,0)	$3z^2-r^2$
	5	(0,0,0)	x^2-y^2
Oxygen p	6	$\frac{1}{2}a(1,0,0)$	x_1
	7	$\frac{1}{2}a(1,0,0)$	y_1
	8	$\frac{1}{2}a(1,0,0)$	z_1
	9	$\frac{1}{2}a(0,1,0)$	x_2
	10	$\frac{1}{2}a(0,1,0)$	y_2
	11	$\frac{1}{2}a(0,1,0)$	z_2
	12	$\frac{1}{2}a(0,0,1)$	x_3
	13	$\frac{1}{2}a(0,0,1)$	y_3
	14	$\frac{1}{2}a(0,0,1)$	z_3

B. Rhenium-rhenium (*d-d*) interactions

$D_1\equiv E_{xy,xy}(000)$, $D_4\equiv E_{3z^2-r^2,3z^2-r^2}(000)$,
$D_2\equiv E_{xy,xy}(100)$, $D_5\equiv E_{3z^2-r^2,3z^2-r^2}(001)$,
$D_3\equiv E_{xy,xy}(001)$, $D_6\equiv E_{x^2-y^2,x^2-y^2}(001)$.

$H_{1,1}=D_1+2D_2(\cos\xi+\cos\eta)+2D_3\cos\zeta$
$H_{2,2}=D_1+2D_2(\cos\eta+\cos\zeta)+2D_3\cos\xi$
$H_{3,3}=D_1+2D_2(\cos\zeta+\cos\xi)+2D_2\cos\eta$
$H_{4,4}=D_4+2D_5(\frac{1}{4}\cos\xi+\frac{1}{4}\cos\eta+\cos\zeta)+\frac{3}{2}D_6(\cos\xi+\cos\eta)$
$H_{5,5}=D_4+\frac{3}{2}D_5(\cos\xi+\cos\eta)+2D_6(\frac{1}{4}\cos\xi+\frac{1}{4}\cos\eta+\cos\zeta)$
$H_{4,5}=\frac{1}{2}\sqrt{3}(D_5-D_6)(-\cos\xi+\cos\eta)$

C. Oxygen-oxygen (*p-p*) interactions

$A_1\equiv E_{x_1,x_1}(000)$, $B_1\equiv E_{y_1,y_1}(000)$, $C_1\equiv E_{x_1,x_2}(\frac{1}{2}\frac{1}{2}0)$,
$A_2\equiv E_{x_1,x_1}(100)$, $B_2\equiv E_{y_1,y_1}(100)$, $C_2\equiv E_{x_1,y_2}(\frac{1}{2}\frac{1}{2}0)$,
$A_3\equiv E_{x_1,x_1}(010)$, $B_3\equiv E_{y_1,y_1}(010)$, $C_3\equiv E_{y_1,x_2}(\frac{1}{2}\frac{1}{2}0)$,
$B_4\equiv E_{y_1,y_1}(001)$, $C_4\equiv E_{z_1,z_2}(\frac{1}{2}\frac{1}{2}0)$.

$H_{6,6}=A_1+2A_2\cos\xi+2A_3(\cos\eta+\cos\zeta)$
$H_{7,7}=B_1+2B_2\cos\xi+2B_3\cos\eta+2B_4\cos\zeta$
$H_{8,8}=B_1+2B_2\cos\xi+2B_3\cos\zeta+2B_4\cos\eta$
$H_{9,9}=B_1+2B_2\cos\eta+2B_3\cos\xi+2B_4\cos\zeta$
$H_{10,10}=A_1+2A_2\cos\eta+2A_3(\cos\zeta+\cos\xi)$
$H_{11,11}=B_1+2B_2\cos\eta+2B_3\cos\zeta+2B_4\cos\xi$
$H_{12,12}=B_1+2B_2\cos\zeta+2B_3\cos\xi+2B_4\cos\eta$
$H_{13,13}=B_1+2B_2\cos\zeta+2B_3\cos\eta+2B_4\cos\xi$
$H_{14,14}=A_1+2A_2\cos\zeta+2A_3(\cos\xi+\cos\eta)$

$H_{6,9}=4C_1\cos\frac{1}{2}\xi\cos\frac{1}{2}\eta$, $H_{8,12}=-4C_3\sin\frac{1}{2}\xi\sin\frac{1}{2}\zeta$,
$H_{6,10}=-4C_2\sin\frac{1}{2}\xi\sin\frac{1}{2}\eta$, $H_{8,14}=4C_1\cos\frac{1}{2}\xi\cos\frac{1}{2}\zeta$,
$H_{6,12}=4C_1\cos\frac{1}{2}\xi\cos\frac{1}{2}\zeta$, $H_{9,12}=4C_4\cos\frac{1}{2}\eta\cos\frac{1}{2}\zeta$,
$H_{6,14}=-4C_2\sin\frac{1}{2}\xi\sin\frac{1}{2}\zeta$, $H_{10,13}=4C_1\cos\frac{1}{2}\eta\cos\frac{1}{2}\zeta$,
$H_{7,9}=-4C_3\sin\frac{1}{2}\xi\sin\frac{1}{2}\eta$, $H_{10,14}=-4C_2\sin\frac{1}{2}\eta\sin\frac{1}{2}\zeta$,
$H_{7,10}=4C_1\cos\frac{1}{2}\xi\cos\frac{1}{2}\eta$, $H_{11,13}=-4C_3\sin\frac{1}{2}\eta\sin\frac{1}{2}\zeta$,
$H_{7,13}=4C_4\cos\frac{1}{2}\xi\cos\frac{1}{2}\zeta$, $H_{11,14}=4C_1\cos\frac{1}{2}\eta\cos\frac{1}{2}\zeta$.
$H_{8,11}=4C_4\cos\frac{1}{2}\xi\cos\frac{1}{2}\eta$,

D. Oxygen-rhenium (*p-d*) interactions

$P_1\equiv E_{x_2,xy}(0\frac{1}{2}0)$, $P_2\equiv E_{z_3,3z^2-r^2}(00\frac{1}{2})$.

$H_{7,1}=2iP_1\sin\frac{1}{2}\xi$, $H_{9,1}=2iP_1\sin\frac{1}{2}\eta$,
$H_{11,2}=2iP_1\sin\frac{1}{2}\eta$, $H_{13,2}=2iP_1\sin\frac{1}{2}\zeta$,
$H_{8,3}=2iP_1\sin\frac{1}{2}\xi$, $H_{12,3}=2iP_1\sin\frac{1}{2}\zeta$,
$H_{6,4}=-iP_2\sin\frac{1}{2}\xi$, $H_{10,4}=-iP_2\sin\frac{1}{2}\eta$,
$H_{14,4}=2iP_2\sin\frac{1}{2}\zeta$, $H_{6,5}=\sqrt{3}iP_2\sin\frac{1}{2}\xi$,
$H_{10,5}=-\sqrt{3}iP_2\sin\frac{1}{2}\eta$.

---

[13] A. H. Kahn and A. J. Leyendecker, Phys. Rev. **135**, A1321 (1964).

[14] J. M. Honig, J. O. Dimmock, and W. H. Kleiner, J. Chem. Phys. (to be published).

TABLE IV. Dependence of particular energy-band states on individual tight-binding parameters.

No.	State	A_1	A_2	A_3	B_1	B_2	B_3	B_4	C_1	C_2	C_3	C_4	D_1	D_2	D_3	D_4	D_5	D_6	P_1	P_2
1	Γ_{25}				Yes	Yes	Yes	Yes				Yes								
2	Γ_{15}	Yes	Yes	Yes	Yes	Yes	Yes	Yes	Yes			Yes								
1	$\Gamma_{25'}$												Yes	Yes	Yes					
1	Γ_{12}															Yes	Yes	Yes		
2	X_1	Yes	Yes	Yes												Yes	Yes	Yes		Yes
1	X_2															Yes	Yes	Yes		
1	X_3												Yes	Yes	Yes					
2	X_5				Yes	Yes	Yes	Yes					Yes		Yes				Yes	
1	$X_{3'}$				Yes	Yes	Yes	Yes				Yes								
1	$X_{4'}$				Yes	Yes	Yes	Yes				Yes								
2	$X_{5'}$	Yes	Yes		Yes	Yes	Yes	Yes	Yes											
2	M_1	Yes	Yes							Yes						Yes	Yes	Yes		Yes
2	M_2	Yes	Yes							Yes						Yes	Yes	Yes		Yes
2	M_3				Yes	Yes	Yes	Yes			Yes		Yes	Yes	Yes				Yes	
1	M_4				Yes	Yes	Yes	Yes			Yes									
2	M_5				Yes	Yes	Yes	Yes					Yes		Yes				Yes	
1	$M_{4'}$	Yes	Yes	Yes																
1	$\mathrm{M}_{5'}$				Yes	Yes	Yes	Yes												
1	R_1	Yes	Yes	Yes						Yes										
2	R_{12}	Yes	Yes	Yes						Yes						Yes	Yes	Yes		Yes
2	$R_{25'}$				Yes	Yes	Yes	Yes			Yes		Yes	Yes	Yes				Yes	
1	$R_{15'}$				Yes	Yes	Yes	Yes			Yes									

agonal matrix elements of the $2p\pi$ orbitals. The parameters C_1–C_4 introduce off-diagonal nearest-neighbor π-π (C_3,C_4), σ-σ (C_2), and σ-π (C_1) interactions in the Hamiltonian matrix.

By applying the appropriate unitary transformations, the 14×14 Hamiltonian matrix of Table III can be reduced to a considerable extent at the symmetry points Γ, X, M, and R. From the results of Table I, we verify that the dimensions of these reduced submatrices are either 1×1 or 2×2. For the 1×1 cases, the energy of the particular state is linearly related to the tight-binding parameters. The 2×2 solutions are nonlinear functions of the parameters.

The dependence of particular energy levels for the ReO$_3$ structure on the various tight-binding parameters of Table III is summarized in Table IV. The number of states of a particular symmetry is indicated in the first column. Those parameters which are involved in determining the energy of a given energy-band state are indicated by the word yes. The actual coefficients are readily determined from the results of Table III and the appropriate unitary transformations.[13]

According to the results of Table IV, a total of 32 energy levels are available for determining the 19 LCAO parameters. Twelve states occur only once; these provide 12 linear relationships between the energy and the parameters. Ten additional linear equations can be obtained by applying the diagonal sum rule to those states which occur twice. These 22 linear equations (which include only 16 parameters, since C_1, P_1, and P_2 are not involved) are not linearly independent. They can be made linearly independent by eliminating the parameter D_2. When this is done, the remaining 15 parameters can be determined by a least-squares-fitting procedure. Finally, the last four parameters (C_1, D_2, P_1, and P_2) are determined from the nonlinear equations, which represent the difference in energy between those states which occur twice in Table IV.

Only the magnitudes of C_1, P_1, and P_2 are determined by this procedure, since the equations involve the squares of these parameters. Symmetry arguments based on the two-center approximation to these parameters suggest positive signs for C_1 and P_1 and a negative sign for P_2.

This tight-binding scheme is readily extended to include the effects of spin-orbit coupling. Such effects are important only for the rhenium $5d$ states. For example, Herman and Skillman estimate that the spin-orbit effects for oxygen $2p$ states are smaller by at least an order of magnitude.[12] Spin-orbit coupling between the rhenium $5d$ states is introduced by means of an additional parameter, the spin-orbit parameter ξ_{5d}. The appropriate matrix elements of the spin-orbit operator among d states have been tabulated by Friedel *et al.*[15] These effects double the size of the secular equation, increasing it from a 14×14 to a 28×28 equation. As we shall describe later, the final value for the spin-orbit parameter ξ_{5d} was determined by optimizing the theoretical fit to the experimental Fermi-surface data.

III. RESULTS

The general nature of the APW results and the influence of the muffin-tin corrections on the ReO$_3$ band structure are illustrated in Figs. 2(a) and 2(b). Here we plot the energy bands along the Δ direction of the Brillouin zone. The results of Fig. 2(a) were obtained using the muffin-tin potential $V_m(\mathbf{r})$ while those of Fig. 2(b) involved $V_m(\mathbf{r})+V_\Delta(\mathbf{r})$. The energy scale is relative to the constant portion of the muffin-tin potential V_{mo}. Since the APW calculations were carried out only at

---

[15] J. Friedel, P. Lenglart, and G. Leman, J. Phys. Chem. Solids **25**, 781 (1964).

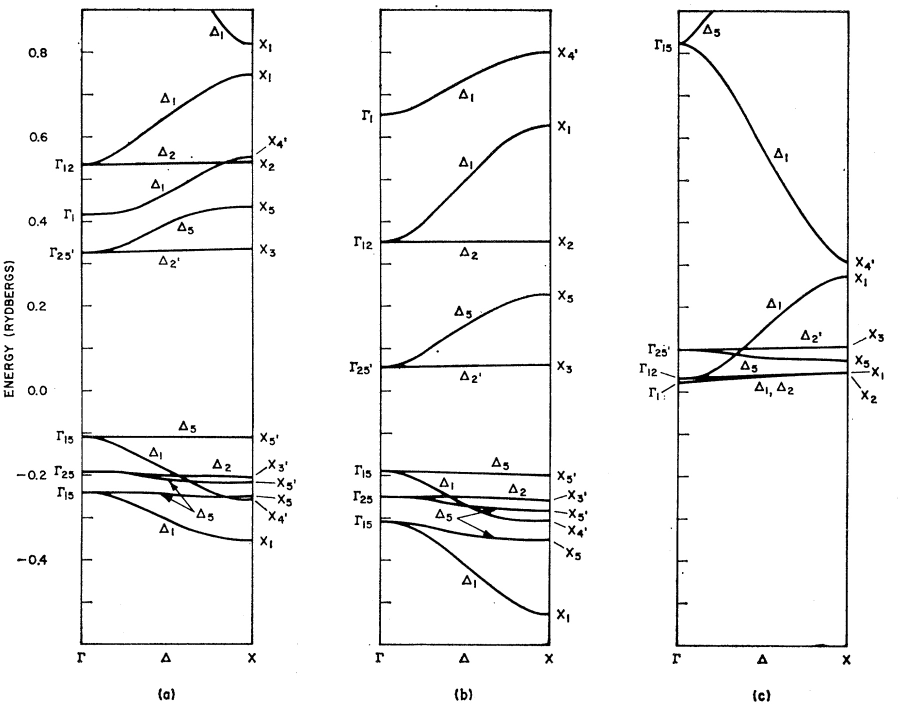

FIG. 2. (a) APW results for ReO_3 along the Δ line involving the muffin-tin potential $V_m(\mathbf{r})$. (b) Corresponding results obtained by adding corrections $V_\Delta(\mathbf{r})$ to the muffin-tin potential $V_m(\mathbf{r})$. (c) APW results involving $V_m(\mathbf{r})+V_\Delta(\mathbf{r})$, in which $V_m(\mathbf{r})$ is set equal to zero within the oxygen spheres.

symmetry points, the connecting bands are meant to illustrate the connectivity required by the compatibility relations rather than the detailed band shapes.

In Figs. 2(a) and 2(b), the lowest nine bands correspond to oxygen $2p$ states. This is easily established by comparing with the results of Table I. These oxygen $2p$ bands are separated by an energy gap from three distinct groups of bands. These include the rhenium $5d$ bands plus some s-p or nearly-free-electron–type bands. The rhenium $5d$ bands are separated into t_{2g} ($\Gamma_{25'}$; X_3, X_5) and e_g (Γ_{12}; X_2,X_1) manifolds. The nearly-free-electron bands connect Γ_1, $X_{4'}$, and presumably the highest X_1 state in Fig. 2(a).

From these results, it is clear that the corrections to the muffin-tin potential have an important effect on the ReO_3 band structure. These corrections shift groups of bands by energies as large as ±0.25 Ry. These shifts reduce the oxygen-rhenium ($2p$-$5d$) band gap by almost 50% and place the s-p band above the e_g manifold. These corrections also increase the magnitude of the oxygen-rhenium ($2p$-$5d$) hybridization interaction. This affects the oxygen $2p$ bandwidth as well as the corresponding bandwidths of the t_{2g} and e_g manifolds.

In order to indicate the over-all effect of oxygen-rhenium hybridization on the ReO_3 conduction bands, an additional APW calculation involving $V_m(\mathbf{r})+V_\Delta(\mathbf{r})$ has been carried out. In this calculation, the potential within the oxygen muffin-tin spheres was set equal to zero (V_{mo}). The corresponding energy-band results along the Δ direction are shown in Fig. 2(c). As expected, the nine oxygen $2p$ bands have disappeared. In addition, this modification to the oxygen potential has produced important changes in the conduction bands. The rhenium $6s$-$6p$ bands (Γ_1,Γ_{15}; X_1,$X_{4'}$) have shifted to lower energies so that Γ_1 lies slightly below the bottom of the $5d$ bands. Equally interesting and important is the fact that the ordering of the Γ_{12} and $\Gamma_{25'}$ states has been reversed and both the e_g and t_{2g} bandwidths have been reduced significantly by this modification.

The results of APW calculations at the symmetry points Γ, X, M, and R involving $V_m(\mathbf{r})+V_\Delta(\mathbf{r})$ [Fig. 2(b)] have been used to determine the LCAO tight-binding parameters defined in Table III, following the procedures described in Sec. II C. The values obtained for these parameters are listed in Table V under the "Fitted" heading. The two-center representation of these parameters is contained in the last column. Here, the subscripts 1 and 2 refer to nearest- and next-nearest-neighbor interactions.

If these parameters are introduced into the Hamiltonian matrix of Table III and the resulting secular equation is diagonalized, the energy-band curves shown in Fig. 3(a) are obtained. The solid lines correspond to the LCAO results while the open circles represent the APW values. The LCAO interpolation scheme succeeds in ordering correctly all states at symmetry points as a function of energy. The poorest fit involves the strongly hybridized states such as X_1, M_1, M_2, and R_{12}. In these cases, the interpolated results are in error by as much as 0.04 Ry. In general, the fit is accurate to better than 0.01 Ry. A detailed comparison between the APW and LCAO results at symmetry points in the Brillouin zone is contained in Table VI.

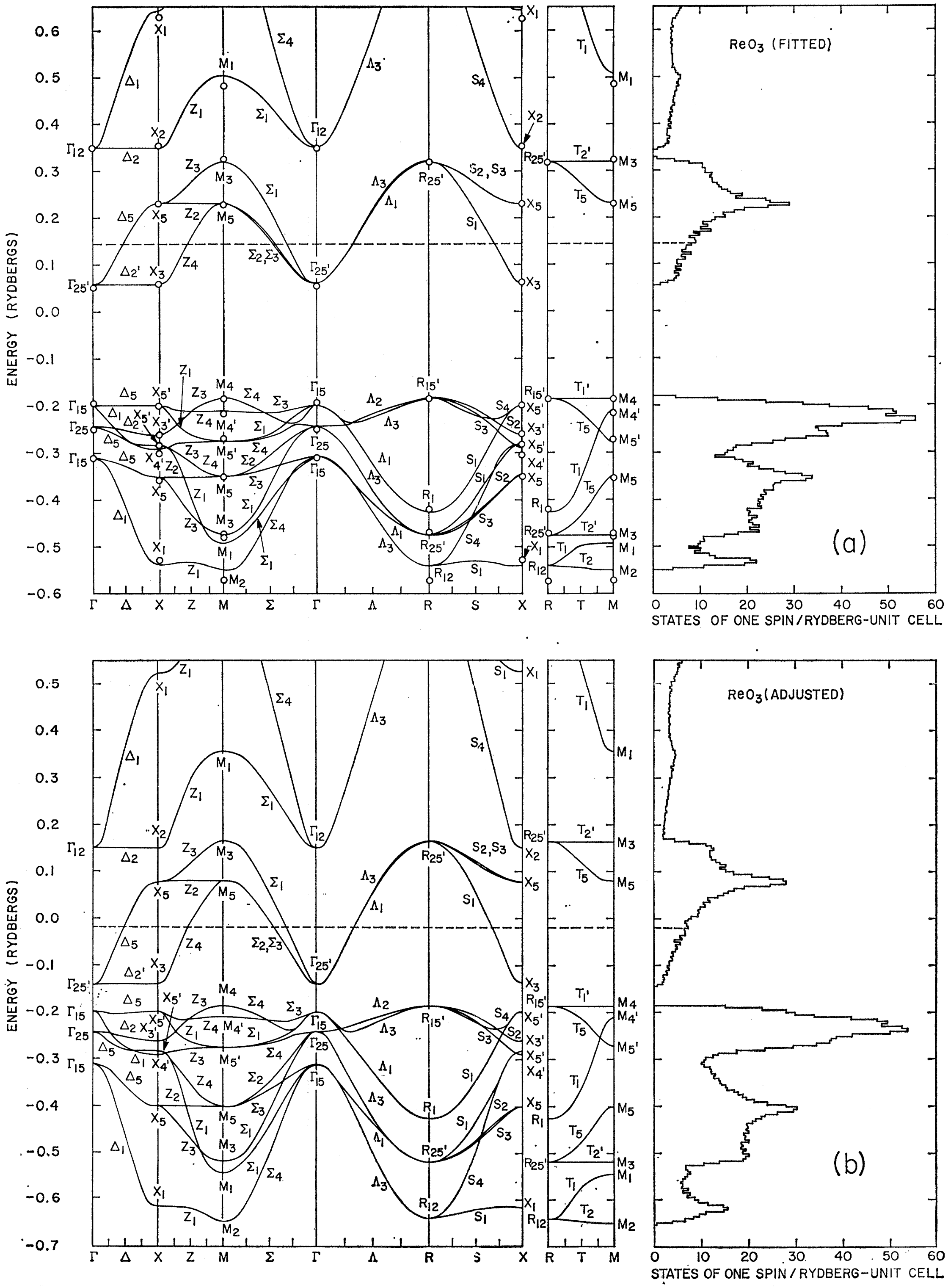

Fig. 3. (a) Tight-binding energy bands for ReO$_3$ obtained by fitting APW results at symmetry points. (b) Adjusted band structure for ReO$_3$.

TABLE V. Values for the fitted and adjusted ReO_3 tight-binding parameters (in rydbergs). Column 4 contains the two-center approximation to these parameters.

	Fitted	Adjusted	Two-center approximation
A_1	−0.2761	−0.2761	p_0
A_2	0.0258	0.0258	$(pp\sigma)_2$
A_3	−0.0034	−0.0034	$(pp\pi)_2$
B_1	−0.2294	−0.2294	p_0
B_2	−0.0191	−0.0191	$(pp\pi)_2$
B_3	0.0049	0.0049	$(pp\sigma)_2$
B_4	−0.0001	−0.0001	$(pp\pi)_2$
C_1	0.0097	0.0097	$\frac{1}{2}(pp\sigma)_1+\frac{1}{2}(pp\pi)_1$
C_2	0.0142	0.0142	$\frac{1}{2}(pp\sigma)_1-\frac{1}{2}(pp\pi)_1$
C_3	0.0034	0.0034	$\frac{1}{2}(pp\sigma)_1-\frac{1}{2}(pp\pi)_1$
C_4	−0.0037	−0.0037	$(pp\pi)_1$
D_1	0.0592	−0.1408	d_0
D_2	0.0000	0.0000	$(dd\pi)_1$
D_3	−0.0001	−0.0001	$(dd\delta)_1$
D_4	0.4218	0.2218	d_0
D_5	−0.0241	−0.0241	$(dd\sigma)_1$
D_6	0.0006	0.0006	$(dd\delta)_1$
P_1	0.1324	0.1200	$(pd\pi)_1$
P_2	−0.2210	−0.2450	$(pd\sigma)_1$
ξ_{5d}		0.0350	

The density-of-states curve for this band structure is represented by the histogram to the right. This curve has been obtained by sampling the equivalent of 64 000 uniformly distributed points in the Brillouin zone. The actual calculations were confined to 1/48 of the Brillouin zone, as shown in Fig. 1(b). The density-of-states curve exhibits a considerable amount of structure, particularly in the oxygen $2p$ valence bands. A single peak due to the flat Z_2 band dominates the density-of-states curve in the conduction band.

The ReO_3 Fermi energy is indicated by the horizontal dashed line. It occurs in the t_{2g} manifold originating from $\Gamma_{25'}$. These bands do not quite overlap the e_g bands which evolve from Γ_{12}. According to the results of Fig. 2(c), the energy splitting between Γ_{12} and $\Gamma_{25'}$ is due to oxygen-rhenium ($2s$-$5d$) hybridization effects. The present calculations predict a splitting of about 0.3 Ry or 4 eV.

TABLE VI. Comparison between the calculated APW and fitted LCAO tight-binding results at symmetry points in the Brillouin zone.

State	APW	LCAO	State	APW	LCAO
Γ_1	0.6532	···	M_2	0.8105	0.7748
Γ_{12}	0.3511	0.3514	M_1	0.4868	0.5057
$\Gamma_{25'}$	0.0546	0.0591	M_3	0.3275	0.3209
Γ_{15}	−0.1929	−0.1979	M_5	0.2291	0.2299
Γ_{25}	−0.2502	−0.2434	M_4	−0.1864	−0.1878
Γ_{15}	−0.3110	−0.3129	$M_{4'}$	−0.2177	−0.2109
			$M_{5'}$	−0.2701	−0.2773
X_1	0.6260	0.6457	M_5	−0.3500	−0.3517
X_2	0.3563	0.3490	M_3	−0.4740	−0.4765
X_5	0.2300	0.2296	M_1	−0.4797	−0.4943
X_3	0.0638	0.0593	M_2	−0.5714	−0.5512
$X_{5'}$	−0.1999	−0.1989			
$X_{3'}$	−0.2599	−0.2631	R_{12}	0.8030	0.7757
$X_{5'}$	−0.2823	−0.2833	$R_{25'}$	0.3215	0.3212
$X_{4'}$	−0.3028	−0.2924	$R_{15'}$	−0.1887	−0.1873
X_5	−0.3533	−0.3520	R_1	−0.4207	−0.4277
X_1	−0.5321	−0.5393	$R_{25'}$	−0.4726	−0.4762
			R_{12}	−0.5740	−0.5411

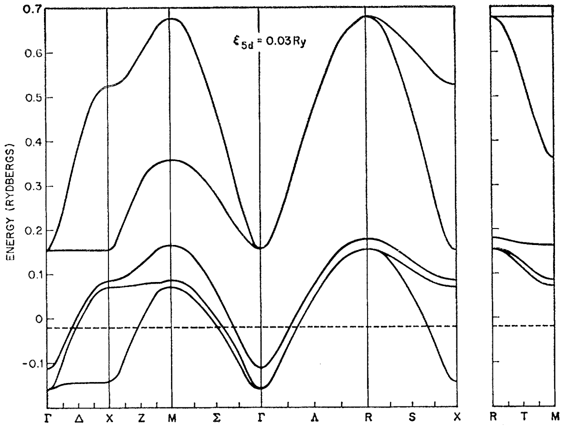

FIG. 4. Conduction bands in ReO_3 including spin-orbit coupling.

The t_{2g} and e_g bandwidths are due almost entirely to (p-d) hybridization effects, which are very strong in ReO_3. This is reflected by the large values for P_1 and P_2 in Table V. Typical bandwidths expected from rhenium-rhenium (d-d) overlap effects are much smaller, as the results of Fig. 2(c) indicate.

The energy-band results shown in Fig. 3(b) were obtained using the parameters listed in Table V under the "Adjusted" heading (but neglecting spin-orbit effects). As described in the following sections, these adjustments were introduced in order to provide a more accurate representation of both the experimental Fermi surface as well as the optical data. The main effect of these adjustments on the band structure is to decrease the energy gap between the oxygen $2p$ and rhenium $5d$ bands and to accentuate the hybridization effects. The density-of-states curve shown to the right in Fig. 3(b) represents 125 000 points in the Brillouin zone. It shows slightly less scatter than the corresponding curve in Fig. 3(a), but still reflects the same general features.

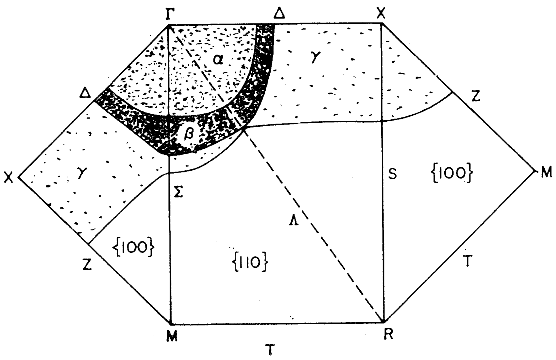

FIG. 5. Central {110} and {100} cross sections of the ReO_3 Fermi surface.

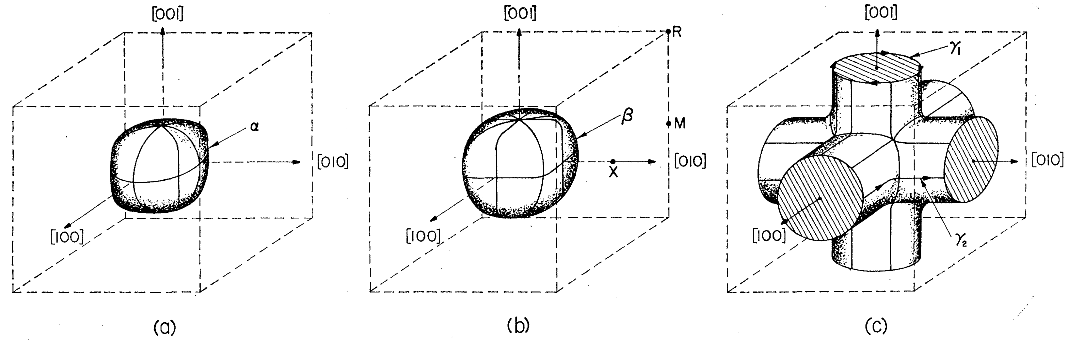

FIG. 6. Three-dimensional sketch of the α(a), β(b), and γ(c) sheets of the ReO$_3$ Fermi surface.

The effects of spin-orbit coupling on the rhenium $5d$ conduction bands are shown in Fig. 4 for $\xi_{5d}=0.030$ Ry. As expected, spin-orbit effects reduce many degeneracies at symmetry points and eliminate most band-crossings along symmetry lines. Spin-orbit effects split the $\Gamma_{25'}$ state into a lower fourfold degenerate Γ_{8+} state and an upper doubly-degenerate Γ_{7+} state. Neglecting the interaction with the higher Γ_{8+} state which originates from Γ_{12}, the $[E(\Gamma_{7+})-E(\Gamma_{8+})]$ splitting is $\frac{3}{2}\xi_{5d}$.[16] Similar splittings occur at the symmetry point R; however, these are reduced by oxygen-rhenium ($2p$-$5d$) hybridization effects. This hybridization is sufficiently strong to transfer reduced spin-orbit splittings to the oxygen $2p$ bands. Except along the Λ direction, all the bands shown in Fig. 4 are nondegenerate (neglecting spin). The lower and upper bands drawn along the Λ direction actually correspond to pairs of bands. These pairs are nearly degenerate and are separated by energies in the 0.0001–0.004 Ry range.

Central cross sections of the ReO$_3$ Fermi surface that are obtained from the band structure of Fig. 4 are shown in Fig. 5. The rectangular portion of this figure (ΓMRX) corresponds to a central $\{110\}$ cross section. The two triangular sections (ΓMX and XRM) represent central $\{100\}$ planes, one through Γ and the other through X.

The three sheets of the ReO$_3$ Fermi surface are labelled α, β, and γ, respectively. Each sheet corresponds to an electronlike surface centered about Γ. The α and β sheets are closed, while the γ sheet is open along $\langle 100\rangle$. Because of the nearly degenerate bands along the Λ direction in Fig. 4, the β and γ sheets nearly touch along $\langle 111\rangle$. The α Fermi surface sheet contains 0.093 electrons per rhenium atom. The β and γ sheets contain 0.171 and 0.736 electrons per atom, respectively.

Three-dimensional sketches of these Fermi-surface sheets are shown in Figs. 6(a)–6(c), respectively. The α sheet is rather circular in the $\{100\}$ planes and slightly squared-off in the $\{110\}$ planes. The reverse is true for the β sheet. According to Figs. 5 and 6(c), the open sheet consists of three intersecting cylinders. Two closed extremal orbits which exist on γ when the magnetic field is along [001] are shown in Fig. 6(c). The electronlike orbit labelled γ_1 exists on the arms of the cylinder and is centered about X. The holelike orbit labelled γ_2, which is closed in the extended zone scheme, is centered about the point M. Another extremal orbit γ_3 [which is not shown in Fig. 6(c)] exists on the γ sheet when the magnetic field is near $\langle 111\rangle$.

The angular variation of central extremal areas and cyclotron masses for orbits on the ReO$_3$ Fermi-surface have been determined via the Mueller inversion scheme.[17] Figure 7 contains the results for magnetic field directions in $(1\bar{1}0)$ and (001) planes, respectively. The procedures and techniques involved in these calculations will be described in detail elsewhere.[18] The

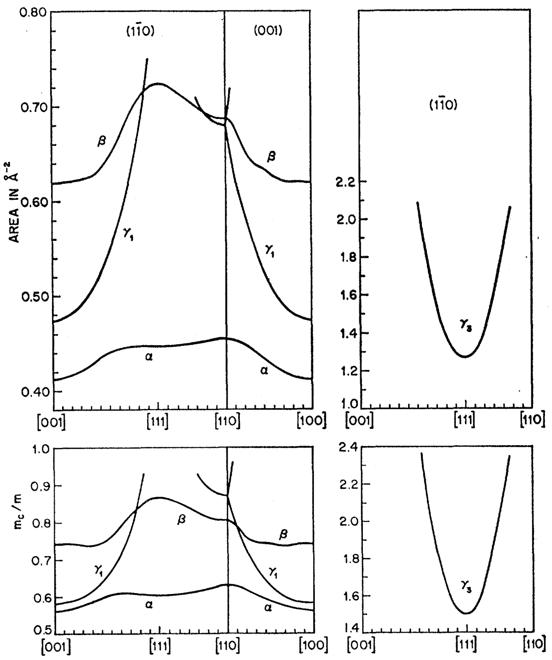

FIG. 7. Extremal areas and cyclotron masses for closed orbits on the ReO$_3$ Fermi surface.

---

[16] L. F. Mattheiss, Phys. Rev. **139**, A1893 (1965).

[17] F. M. Mueller, Phys. Rev. **148**, 636 (1966).

[18] L. F. Mattheiss (unpublished).

present discussion is limited to a brief summary of the methods employed.

The Mueller inversion scheme is used here to convert calculated values of the Fermi radii $[k_\alpha(\theta,\varphi)$, $k_\beta(\theta,\varphi)$, and $k_\gamma(\theta,\varphi)$ with an origin at $\Gamma]$ to extremal cross-sectional areas. Somewhere between 40 and 50 values of $[k_\nu(\theta_i,\varphi_i)]^2$ are fit with 12–16 Kubic harmonics using least-squares techniques. By calculating the area $A_\nu(\theta,\varphi)$ as a function of energy E, the cyclotron mass,

$$\frac{m_c}{m}=\frac{\hbar^2}{2\pi m}\frac{\partial A(\theta,\varphi)}{\partial E}\bigg|_{E=E_F}, \qquad (5)$$

is readily determined by numerical differentiation.

The application of this method to the closed α and β sheets is straightforward. However, the open γ sheet presents more of a problem. Following the suggestion of Zornberg and Mueller,[19] we "close" this sheet by adding a fictitious "tip." Although the resulting surface is highly anisotropic, the inversion scheme seems to work satisfactorily. The fictitious tip is actually determined by the inversion scheme, since the Fermi radii $[k_\gamma(\theta_i,\varphi_i)]^2$ are chosen to avoid the neck region entirely. The γ_1 orbits on the open sheet of the Fermi surface are determined in a similar manner, using the point X $(0,0,\pi/a)$ as an origin. In this case, the inversion scheme converts the arms of the γ Fermi-surface sheet into a "capped" cylindrical-type surface. These artificially closed surfaces appear to provide accurate results except when the orbit passes over or near the fictitious regions.

According to the results of Fig. 7, the areas of α and β branches are fairly isotropic. The area of the γ_1 branch increases like $\sec\theta$, where θ is measured from [100]. This orbit is expected to disappear at approximately $\theta=45°$, when the orbit begins to extend onto the Γ-centered body of the γ Fermi surface sheet. According to the preceding discussion, this is precisely the region where the inversion results become unreliable. We conclude that the γ_1 results are probably not very accurate in this limiting region. The same is true for the γ_3 results shown to the right in Fig. 7. As the magnetic field is rotated from [111] toward either [001] or [110], the orbit extends onto the arms of the γ Fermi-surface sheet and approaches the fictitious tip centered at X.

There are some additional orbits which are not included in the results shown in Fig. 7. The first is represented by γ_2 in Fig. 6(c). By direct calculation, this orbit encloses an area of 0.808 Å^{-2} and has a cyclotron mass of -0.87 m. Another possible orbit involves magnetic breakdown from the β to the γ Fermi-surface sheets when the magnetic field is near $\langle 110\rangle$. The extremal area and cyclotron mass of this orbit are found to be 0.750 Å^{-2} and 0.86 m, respectively. A third set of closed orbits can exist on the γ sheet. These are holelike orbits whose plane passes through the symmetry point R in Fig. 6. They are analogous to the γ_3 orbits of Fig. 7. We have not calculated either the area or the cyclotron mass of this set of orbits.

IV. COMPARISON WITH EXPERIMENT

The de Haas–van Alphen data of Marcus[5] and the optical data of Feinleib *et al.*[4] have been used to adjust the original APW model for the ReO_3 band structure. In general terms, our interpretation of the optical data suggests that the oxygen-rhenium ($2p$-$5d$) energy gap shown in Fig. 3(a) should be reduced from 0.25 Ry to about 0.05 Ry. In addition, the cyclotron-mass measurements by Marcus suggest that the $\Gamma_{25'}$-$R_{25'}$ bandwidth of Fig. 3(a) be increased by 10% or so. The adjusted results of Fig. 3(b) reflect both these modifications to the fitted ReO_3 band structure.

A. Fermi-Surface Data

The de Haas–van Alphen data of Marcus are shown by the open and filled circles in Fig. 8. The solid lines represent the Fermi-surface areas obtained from the adjusted band structure of Fig. 4. In the regions where the γ_1 and β branches cross, Marcus makes no specific assignment of areas (or frequencies) with the individual branches. Consequently, the distinction between the open and filled circles is quite arbitrary in these regions.

It was found that the relative dimensions of the α, β, and γ sheets of the Fermi surface were reasonably sensitive to the value of the spin-orbit parameter ξ_{5d}. According to Marcus, the low-frequency oscillations have the largest amplitude; as a result, we assume that this data is the most reliable. We have determined ξ_{5d} by optimizing the theoretical fit to these data. The value $\xi_{5d}=0.030$ Ry was obtained in this manner (Table V and Fig. 4). With this value for ξ_{5d}, the theoretically determined area as a function of angle for the α sheet of the Fermi surface fits the de Haas–van Alphen data to within 5%, as shown by Fig. 8.

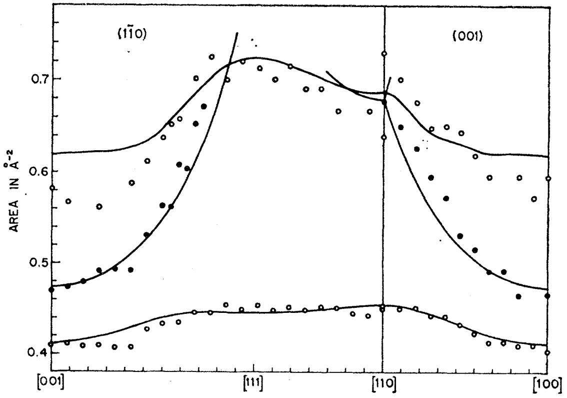

FIG. 8. Comparison between the de Haas–van Alphen results of Marcus (open and filled circles) and the present theoretical model (solid lines).

---

[19] E. I. Zornberg and F. M. Mueller, Phys. Rev. **151**, 557 (1966).

The corresponding data for the γ_1 branch also agrees with the theoretical curve to within about 5%. The fit to the cross-sectional area of the orbit centered about X on the arms of the γ sheet when the magnetic field is along [001] is particularly good. However, the data appear to rise more rapidly than the theoretical curve as the magnetic field is rotated away from [001] in either the (100) or the (1$\bar{1}$0) plane. This suggests that the arms of the γ sheet are more tapered than the calculations predict.

The fit of the experimental data to the theoretical curve for the β sheet is the least accurate, with deviations as large as 10%. Since these oscillations have the smallest amplitude,[5] the data is presumably less reliable. In general, the angular variation of the data agrees well with the calculated curve.

Marcus has determined the cyclotron masses for several orbits on the α sheet of the Fermi surface. These are compared with the calculated results in Table VII. For comparison purposes, we include the cyclotron masses predicted by the fitted as well as the adjusted band-structure models for ReO$_3$. As mentioned previously, the discrepancy between the fitted results and the experimental values was one of the factors which was taken into account in the adjustment procedure.

Additional Fermi-surface data for ReO$_3$ has been obtained from magnetothermal oscillations by Graebner.[6] By combining field sweep and rotation data, Graebner is able to determine the angular variation of Fermi-surface areas more precisely. In general, the data are consistent with Marcus's de Haas–van Alphen results.

B. Optical Data

Feinleib *et al.*[4] have measured the reflectance of ReO$_3$ over a 22-eV energy range. They have analyzed their reflectance data by the Kramers-Kronig relations to determine the real and imaginary parts of the dielectric constant $\epsilon_1(\omega)$ and $\epsilon_2(\omega)$, respectively. They obtain an $\epsilon_2(\omega)$ curve which exhibits free-electron characteristics below about 2.3 eV, where interband transitions begin. They find principal peaks in ϵ_2 at 4.2, 9.3, and 14 eV, with some smaller structure at 7.0 and 8.5 eV. The structure above 2.3 eV is attributed to interband transitions by these authors.

In the present investigation, we have applied the simplest possible model for interpreting the structure in the ϵ_2 curve for ReO$_3$. This model ignores the transition-probability matrix elements and involves only a calculation of the joint density of states $J_{n,s}(\omega)$, where

$$J_{n,s}(\omega)=\frac{2}{(2\pi)^3}\int_{\omega_{n,s}(\mathbf{k})=\omega}\frac{ds}{|\nabla_k\omega_{n,s}(\mathbf{k})|}, \qquad (6)$$

$\hbar\omega_{n,s}(\mathbf{k})=E_s(\mathbf{k})-E_n(\mathbf{k})$, ds is an element of area on the surface for which $\omega_{n,s}(\mathbf{k})=\omega$, and n and s refer to occupied and unoccupied states, respectively.[20]

TABLE VII. Cyclotron masses for α orbits on the ReO$_3$ Fermi surface with the magnetic field near ⟨111⟩ in a {1$\bar{1}$0} plane.

H	Experiment[a] m_c/m	Fitted m_c/m	Adjusted m_c/m
⟨111⟩−9°	0.68	0.758	0.637
⟨111⟩	0.67	0.757	0.635
⟨111⟩+17°	0.65	0.759	0.645

[a] Reference 5.

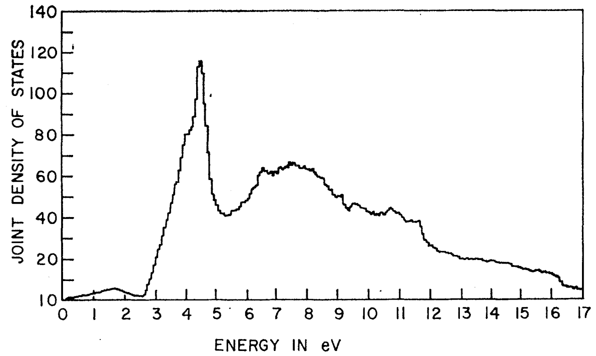

FIG. 9. Joint density-of-states curve for the adjusted band structure of Fig. 3(b).

The joint density-of-states curve which is obtained from the adjusted band structure of Fig. 3(b) is shown in Fig. 9. Spin-orbit effects have been neglected in this calculation. The curve has been obtained by sampling the equivalent of 125 000 uniformly distributed points in the Brillouin zone. These points are identical with those used to determine the density-of-states curve in Fig. 3(b).

The main features of this joint density-of-states curve are a large narrow peak centered near 3.5 eV plus a fairly broad peak extending from approximately 6–12 eV. The general shape of the joint density-of-states curve resembles the valence band density-of-states curve in Fig. 3(b). This similarity may be due to the peak in the conduction-band density of states at 0.075 Ry, which results from the (X_5-M_5) degeneracy. It appears that this peak serves to pick out the structure in the valence-band density of states.

In view of the simplified model introduced here to interpret the ReO$_3$ optical data, we have concentrated our attention on one feature of the data, namely, the low-energy peak in ϵ_2 at 4.2 eV. The fitted band structure of Fig. 3(a) produced a joint density of states similar to that shown in Fig. 9 except that the first large peak occurred near 6.5 rather than 4.5 eV. The fitted parameters were adjusted to lower this peak by about 2 eV.

The experimental ϵ_2 curve contains additional peaks, one extending from about 8–12 eV and the other centered near 14 eV. In terms of the joint density-of-states model, these peaks tower over the 4.2-eV peak in

---

[20] David Brust, Phys. Rev. **134**, A1337 (1964).

height. The 9.3-eV peak is about three times larger than the 4.2-eV peak. The 14-eV peak is roughly five times larger. According to Fig. 9, the present calculations provide a rather poor representation for this high-energy structure in ϵ_2. It is possible that variations in the transition-probability matrix elements are responsible for these differences. More accurate dielectric constant calculations involving the techniques proposed by Dresselhaus and Dresselhaus might resolve these difficulties.[21]

In proposing this interpretation for the ϵ_2 curves for ReO_3, we are encouraged by the fact that a similar interpretation is consistent with Cardona's ϵ_2 curves for the structurally-related compounds $SrTiO_3$ and $BaTiO_3$.[22] In both materials, Cardona finds a peak in ϵ_2 near 5 eV, with a shoulder on the low-energy side. The shape of this peak is quite similar to the one centered about 4.5 eV in Fig. 9. The high-energy structure in ϵ_2 is also in reasonable agreement with this joint density-of-states curve. Of course, the band structures for $SrTiO_3$ and $BaTiO_3$ differ from the present ReO_3 results; however, as we discuss in Sec. V, the band structures for these materials are expected to share many common features.

V. DISCUSSION

The traditional approach to the theory of transition-metal oxides involves the ligand-field and molecular-orbital theories.[23,24] As a result, it is appropriate to begin this discussion of the ReO_3 band structure by establishing a connection between the present energy-band approach and the ligand-field and molecular-orbital theories of transition-metal oxides.

Ligand-field theory treats the transition-metal ions in an electrostatic crystal-field environment which arises from the negatively charged neighboring ligand ions (which are often considered to be negative point charges). This theory neglects completely any covalent bonding or hybridization effects between the transition-metal ion and its neighbors. In an octahedral environment, the electrostatic repulsion due to the negatively charged ligands causes a splitting of the five d orbitals into two separate groups of levels; these consist of $t_{2g}(xy, yz, \text{and } zx)$ and $e_g(3z^2-r^2 \text{ and } x^2-y^2)$ orbitals, respectively. Since the e_g orbitals point in the direction of the ligands, they experience greater electrostatic repulsion than the t_{2g} orbitals. As a result, the t_{2g} level is at a lower energy than the e_g level in such an environment. The energy splitting between the t_{2g} and e_g levels is normally denoted by the parameter $10Dq$.

On the other hand, the molecular-orbital theory is more realistic in that it treats both the transition-metal ion as well as its neighboring ligands directly in terms of symmetrized combinations of atomic-type orbitals. As a result, this theory includes covalency and hybridization effects. In a typical application, this method would be used to treat a single ReO_6 complex, thereby neglecting the effects of lattice periodicity. When the lattice periodicity is taken into account, this molecular-orbital scheme becomes identical with the tight-binding method in solids.

In its simplified form, the results of a molecular-orbital calculation are related to the band structure at the center (Γ) and corner (R) of the Brillouin zone. For an octahedrally coordinated system, this is seen by comparing the bonding and antibonding molecular orbitals[24] with the corresponding LCAO tight-binding functions.[13] Therefore, this molecular-orbital approach is meaningful only when the crystal-field splitting $10Dq$ is large compared to the t_{2g} and e_g bandwidths. The results of Figs. 3(a) and 3(b) suggest that this condition is not satisfied in ReO_3 since the t_{2g} and e_g bandwidths are comparable in magnitude with $10Dq$.

The magnitude of $10Dq$ plays a central role in the ligand-field and molecular-orbital theories. Our discussion is concerned primarily with the strong-field limit, where $10Dq$ is large compared to atomic multiplet splittings and spin-orbit effects. Attempts to calculate $10Dq$ via the ligand-field and molecular-orbital theories have enjoyed only limited success. $KNiF_3$ has been a favorite system for such attempts. Although there is still some controversy, the consensus is that ligand-field effects account for about one-third of $10Dq$ in $KNiF_3$ while the remaining two-thirds are attributed to covalency effects.[24] Our interpretation of the results shown in Figs. 2(a) and 2(b) involves a similar explanation for the $10Dq$ splitting in ReO_3. We attribute the 0.2 Ry contribution to $10Dq$ in the muffin-tin results of Fig. 2(a) to oxygen-rhenium ($2s$-$5d$) covalency effects. In Fig. 2(b), the additional contribution of 0.1 Ry to $10Dq$ is due to the muffin-tin corrections $V_\Delta(\mathbf{r})$, which are analogous to the electrostatic ligand-field effects.

The results of Fig. 2(c) emphasize the crucial effect that oxygen-rhenium covalency has on the ReO_3 conduction bands. Unlike the fcc and bcc transition metals,[25,26] the Γ_{12}-$\Gamma_{25'}$ splitting in Fig. 2(b) is not determined by the two-center (d-d) integrals which are responsible for the over-all d bandwidth. These parameters are responsible for the reduced splitting of opposite sign in Fig. 2(c). The fact that Γ_{12} interacts with the oxygen $2s$ levels is a special feature of the ReO_3 and perovskite structures. It does not occur, for example, in the NaCl or CsCl structures.

The ReO_3 conduction bands also differ from those of the transition metals in that the bottom of the s band Γ_1

---

[21] G. Dresselhaus and M. S. Dresselhaus, Phys. Rev. **160**, 649 (1967).

[22] Manuel Cardona, Phys. Rev. **140**, A651 (1965).

[23] Leslie E. Orgel, *An Introduction to Transition-Metal Chemistry* (Wiley-Interscience, Inc., New York, 1966), 2nd ed.

[24] J. Owen and J. H. M. Thronley, in *Reports on Progress in Physics*, edited by A. C. Stickland (Stonebridge Press, Bristol, England, 1966).

[25] F. M. Mueller, Phys. Rev. **153**, 659 (1967).

[26] R. A. Deegan, Phys. Rev. **171**, 659 (1968).

lies above the d-band states. From the results of Fig. 2 and Table I, it is clear that oxygen-rhenium ($2s$-$6s$) and ($2s$-$6p$) hybridization are responsible for shifting to higher energies the plane-wave–type bands which originate from Γ_1.

The position and width of the oxygen $2s$ bands in ReO$_3$ also suggest strong hybridization effects. On the energy scale of Fig. 2, these bands are centered at -1.4 Ry and have a 0.11 Ry bandwidth. On this same energy scale, the energies of the HFS oxygen $2s$ and $2p$ atomic levels[12] are -1.2 and -0.12 Ry, respectively. Differences between the muffin-tin and atomic potentials could introduce moderate energy shifts in the solid. However, we note that the top of the oxygen $2p$ bands in Fig. 2(a) is close to the atomic $2p$ level while the $2s$ bands are located approximately 0.2 Ry below the oxygen $2s$ atomic level. We attribute this shift to oxygen-rhenium $2s$-$6s$, $2s$-$6p$, and $2s$-$5d$ hybridization. Those oxygen $2s$ band states which interact with the rhenium $5d$ and $6s$ states (Γ_1,Γ_{12}; X_1,X_2; M_1) are all grouped within 0.025 Ry of the bottom of the $2s$ band (Γ_1), while the remaining states which interact with rhenium $6p$ levels ($X_{4'}$; $M_{5'}$; R_{15}) are grouped within 0.005 Ry of the top.

These considerations lead to a closely related question concerning the validity of the ionic model in transition-metal oxides. As described in Sec. II, the starting point of the present APW calculation corresponds to the nonionic limit since it involves an *ad hoc* crystal potential which is derived from neutral atom charge densities. We have not attempted to achieve a self-consistent calculation using, for example, the iteration techniques described by DeCicco.[7] However, we have calculated the charge distribution which is implied by the LCAO eigenvectors. In this calculation, we assume that the orthogonalized orbitals which represent the oxygen $2p$ and rhenium $5d$ states are completely localized about the oxygen and rhenium sites, respectively. With this approximation, we can calculate a separate density of states for the oxygen $2p$ and rhenium $5d$ states, weighting each eigenvalue by the sums of squares of the appropriate eigenvector components. At the Fermi energy, this calculation implies a charge distribution of $(\mathrm{Re}^{+4})\,(\mathrm{O}^{-4/3})_3$ for the band structure of Fig. 3(a) and $(\mathrm{Re}^{+3})\,(\mathrm{O}^{-1})_3$ for that of Fig. 3(b). These results probably set an upper limit for the ionicity of Re and O in ReO$_3$.

There has been considerable speculation regarding the nature of the conduction bands in ReO$_3$ and structurally related compounds such as SrTiO$_3$ and Na$_x$WO$_3$. A good summary of these models is contained in Ref. 4. In molecular-orbital terminology, the present calculations predict a conduction band arising from π bonding between rhenium t_{2g} and oxygen $2p$ orbitals. The t_{2g} bandwidth results from the fact that this bonding is zero at the center of the Brillouin zone but nonzero at the zone boundaries. These results substantiate the interpretation by Ferretti *et al.*[27] of the observed metallic conductivity in ReO$_3$ in terms of this model.

These calculations for ReO$_3$ reproduce many of the essential features in the band-structure model for SrTiO$_3$ that has been derived from a tight-binding calculation by Kahn and Leyendecker.[13] SrTiO$_3$ contains one less electron per unit cell than ReO$_3$. According to the Kahn-Leyendecker model, the 18 valence electrons are just sufficient to fill the nine oxygen $2p$ bands. These are separated by a 3-eV energy gap from the unoccupied t_{2g} manifold of conduction band states. The Kahn-Leyendecker model anticipates the value of the tight-binding approximation in these materials. It also anticipates the importance of hybridization effects in determining the valence and conduction bandwidths.

The similarity in the conduction bands predicted by the two calculations is quite striking. The main differences are in the t_{2g} and e_g bandwidths and the $10Dq$ splitting of $\Gamma_{25'}$ and Γ_{12}. Preliminary APW calculations for SrTiO$_3$ suggest that the Kahn-Leyendecker model underestimates these parameters. The ReO$_3$ valence bands differ, however, in several details from those predicted by the Kahn-Leyendecker model. To some extent, these differences originate from the sign of their two-center oxygen-oxygen $(pp\sigma)$ and $(pp\pi)$ integrals. These calculations also differ regarding the location in the Brillouin zone of the conduction-band minimum. Kahn and Leyendecker predict a conduction-band minimum at X. The present ReO$_3$ (and preliminary SrTiO$_3$) calculations favor a minimum at Γ. These differences depend entirely on the sign of the transfer integral $D_3 \equiv E_{xy,xy}(001)$ of Table III. According to Table V, this integral is equivalent to $(dd\delta)_1$ in the two-center approximation. The present calculations predict a negative rather than a positive sign for D_2. This integral is related directly to the energy difference between $\Gamma_{25'}$ and X_3. In fact,

$$4E_{xy,xy}(001) = E(\Gamma_{25'}) - E(X_3).$$

Using the APW values for $E(\Gamma_{25'})$ and $E(X_3)$ from Table VI, we obtain a value for $E_{xy,xy}(001) = -0.0023$ Ry. This is somewhat larger than the fitted value in Table V, where $D_3 = 0.0001$ Ry. According to the results of Fig. 4, spin-orbit coupling favors a conduction-band minimum at Γ by lowering the energy of Γ_{8^+} with respect to the relativistic counterpart of X_3.

Our earlier discussion concerning the covalent contribution to the $10Dq$ splitting in ReO$_3$ illustrates the limitations of our tight-binding model. The present model represents this $10Dq$ splitting in terms of a ligand-field effect and ignores the covalent contribution entirely. In principle, the LCAO approach can be generalized to include these effects by adding oxygen $2s$ and rhenium $6s$ and $6p$ bands. Adding the oxygen $2s$ states increases the size of the (nonrelativistic) Hamil-

---

[27] A. Ferretti, D. B. Rogers, and J. B. Goodenough, J. Phys. Chem. Solids **26**, 2007 (1965).

TABLE VIII. Comparison of oxygen-oxygen (*p-p*) and oxygen-rhenium (*p-d*) tight-binding parameters (in rydbergs) which have been determined from two separate APW calculations, as described in the text.

	$(APW)_1$	$(APW)_2$
A_1	-0.2761	-0.2443
A_2	0.0258	0.0109
A_3	-0.0034	-0.0026
B_1	-0.2294	-0.2332
B_2	-0.0191	-0.0179
B_3	0.0049	0.0043
B_4	-0.0001	-0.0001
C_1	0.0097	0.0094
C_2	0.0142	0.0214
C_3	0.0034	0.0046
C_4	-0.0037	-0.0040
P_1	0.1324	0.1198
P_2	-0.2210	-0.2476

tonian matrix from 14×14 to 17×17. More important, these improvements increase the number of parameters involved. Consequently, we have not attempted to introduce these effects in our model. A fairly direct method has been used to evaluate the physical basis for this tight-binding parameterization scheme. This method has involved an additional APW calculation in which the rhenium 5*d* bands have been artificially lowered in energy with respect to the oxygen 2*p* bands. This has been achieved by rigidly shifting the logarithmic derivatives for the rhenium *d* states to lower energies.[10] If our tight-binding scheme were rigorously correct, only the rhenium-rhenium (*d-d*) and the oxygen-rhenium (*p-d*) parameters should be affected. However, the results show that the oxygen-oxygen (*p-p*) parameters are also affected. The *p-p* and *p-d* parameters obtained from this calculation are listed in Table VIII under the heading $(APW)_2$. These are compared with the previous results of Table V, $(APW)_1$.

The values assumed for the adjusted parameters P_1 and P_2 of Table V were influenced by the results of Table VIII. A larger value for P_1 would further decrease the cyclotron masses of Fig. 7 and Table VII. In connection with our interpretation of the ReO_3 optical data, a larger value would also produce overlap between the t_{2g} and oxygen 2*p* bands. We have not determined the possible effects of this overlap on the ReO_3 Fermi surface.

Feinleib *et al.*[4] have proposed a model band structure for ReO_3 which is based on a simplified version of the Kahn-Leyendecker scheme. They assume that the Fermi energy occurs within the manifold of the t_{2g} bands and neglect the e_g and oxygen 2*p* bands. According to their interpretation, there is no evidence for interband transitions below about 2 eV in their optical data. Since the Kahn-Leyendecker model permits interband transitions at very low energies, they have investigated the possible effects of spin-orbit coupling on these states. Their model involves a spin-orbit parameter which is comparable with the Fermi energy (measured from the bottom of the t_{2g} band). As a result, spin-orbit–induced splittings are large enough to eliminate the low-energy interband transitions.

In the present model for the ReO_3 band structure, spin-orbit coupling produces rather small effects, as shown by the results of Fig. 4. The nearly degenerate bands which occur in the Λ direction indicate the possibility of magnetic breakdown between the β and γ sheets of the Fermi surface when the magnetic field is along [110]. Thus far, there has been no experimental evidence for such magnetic breakdown effects in ReO_3. The fitted value for the spin-orbit parameter $\xi_{5d}=0.030$ Ry is close to the (interpolated) Herman-Skillman atomic spin-orbit parameter for rhenium,[12] namely, 0.032 Ry. Unlike the ReO_3 band model of Feinleib *et al.*, the present model allows interband transitions down to very low energies. However, the results of Fig. 9 suggest that these low-energy transitions will be weak from a density of states point of view.

VI. ACKNOWLEDGMENTS

I am grateful to S. M. Marcus for communicating his de Haas–van Alphen results prior to publication. I have benefited from numerous discussions with J. H. Condon, particularly those concerned with the calculation of the Fourier coefficients of the potential. Finally, I wish to acknowledge useful conversations with J. E. Graebner, E. O. Kane, M. E. Lines, and J. C. Phillips, concerning various aspects of this investigation.